

An experimental study on retrofitted fiber-reinforced concrete beams using acoustic emission

A. Carpinteri, G. Lacidogna, A. Manuello

Department of Structural Engineering and Geotechnics, Politecnico di Torino, Italy

ABSTRACT: Fiber Reinforced Polymer (FRP) sheets are becoming increasingly important as a structural repair method when the load carrying capacity of deteriorated concrete beams is judged to be inadequate. In this field, the repair process must successfully integrate new materials with the old ones, forming a composite system capable of enduring exposure to service loads, environment and time. In this work, a set of Fiber Reinforced Concrete (FRC) beams has been retrofitted with fiber-reinforced polymer (FRP) sheets in order to improve their loading carrying capacity. These beams have been tested up to failure under three-point bending. During the loading tests, the acoustic emission AE technique has been applied to evaluate the damage evolution. By identifying the complete shape of the signals, the three-dimensional locations of damage sources are determined from the AE sensor records. In this connection, the authors have tuned an original procedure using advanced techniques that are usually applied for the analysis of seismic events.

1 INTRODUCTION

A rather recent development in concrete structure technology is represented by steel fiber-reinforced concrete (FRC). By adding steel fibers while mixing the concrete, a so-called homogeneous reinforcement is created. This does not notably increase the mechanical properties before failure, but governs the post-failure behaviour. Thus, plain concrete, which is a quasi-brittle material, is turned to the pseudo-ductile steel fiber-reinforced concrete. In particular, under flexural loading and after matrix crack initiation, the stresses are supported by the bridging fibers and the bending moments are redistributed (RILEM 2002).

As firstly proposed in our experimental research programme, a set of seven FRC beams has been retrofitted with fiber-reinforced polymer (FRP) sheets in order to improve their loading carrying capacity. The use of strengthening techniques may be required in order to reduce the deformations in serviceability state. In this framework, the choice of the proper rehabilitation technique and the assessment of its performance and durability clearly represents outstanding research points. These beams have been tested up to failure under three-point bending (RILEM 1985). The tests programme has permitted to quantify the effect of the FRP reinforcement on the mechanical response of the tested beams. More specifically, an increase in both strength and stiffness of the structural elements has

been recognized, although such an increase is realized at the expense of a loss in ductility, or capacity of the structure to deflect inelastically while sustaining a load close to its maximum capacity. Concerning the failure modes of the tested beams, both FRP delamination and concrete shear failure have been observed, although FRP delamination was predominant. Such failure modes give rise to a brittle mechanical response, corresponding to snap-back instabilities (Carpinteri 1989, Carpinteri et al. 2006a).

The experimental method based on the Acoustic Emission (AE) technique (Shigeishi & Ohtsu 2001, Grosse et al. 2003) is proved to be highly effective for the structural monitoring of the tested specimens, especially to check and measure the damage evolution. The AE signals reflecting the energy release taking place during the three point bending tests can be recorded and micro-cracking sources can be localised by measuring time delays by means of spatially distributed AE sensors. In this application, the AE activity is analysed using techniques similar to those employed for detection of earthquake source epicentre (Carpinteri et al. 2006b; Colombo et al. 2003).

2 EXPERIMENTAL SETUP

2.1 Material data

A set of FRC beams measuring $1000 \times 150 \times 150 \text{ mm}^3$ were cast and subsequently retrofitted with FRP sheets at the Fracture Mechanics Laboratory of the Politecnico di Torino. The elastic modulus, E_a , the Poisson's ratio, ν_a , the characteristic compressive stress, as well as the fiber content in the FRC beams are summarized in Table 1.

Table 1: Mechanical parameters of the FRC beams.

Young Modulus (E_a)	35 GPa
Poissons's Ratio (ν_a)	0.18
Characteristic compressive stress	90 MPa
Fiber Content	40 Kg/m ³

The reinforcement, externally applied along the lower side of the elements, consists in carbon fiber unidirectional laminate sheets in the form of large flat plates cut into 700 mm long and 100 mm wide elements, having a thickness of 1.4 mm and a Young's modulus of 165 GPa. These sheets have been bonded using an epoxy adhesive on the concrete surface. The mechanical parameters of the FRP sheets are summarized in Table 2.

Table 2: Mechanical parameters of the FRP sheets.

Young's Modulus (E), ASTM D303	165 GPa
Max. tensile strain at failure	1.8%
Tensile strength, ASTM D3039	2300 MPa
Nominal thickness	1.4 mm

2.2 Testing machine and AE equipment

The experimental tests were conducted using a servo-controlled machine (MTS) with a closed-loop control (Fig.1). The three point bending test was realized with a linear actuator (hydraulic jack) with passing stem acting in the middle point of the upper side of the beam element, which was positioned on the base of the frame (see Fig. 1). In particular, two specimens with the same nominal geometric and mechanical properties (TR1 and TR2) are considered and analysed. In both cases we performed the test under displacement control, at the rate of 0.011 mm/min for TR1 and 0.005 mm/min for TR2. In addition, the equipment adopted by the authors consists in six USAM® units used for the AE measurements and six pre-amplified piezoelectric (PZT) AE sensors applied to the external surface of the specimens. Such sensors were calibrated on inclusive frequencies between 50 and 800 kHz. PZT sensors (Fig.1) were used, thereby exploiting the capacity of certain crystals to produce electric signals whenever they are subjected to a mechanical stress.

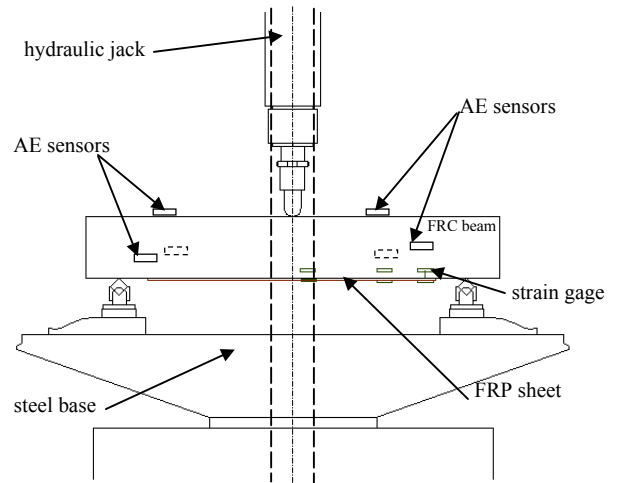


Figure 1. Three point bending experimental setup.

The USAM® units were synchronized for multi-channel data processing. The most relevant parameters acquired from the signals were stored in the USAMs memory and then downloaded to a PC for a multi-channel data processing. From this elaboration micro-crack localisation can be performed. The parameters of a signal recorded by a USAM unit include (Fig.2): the initial instant crossing up-threshold of each P -wave arrival (t_0), the last down-threshold time (t_1) and the number of crossings of the threshold (Fig.3).

The first arrival time at the sensor, S_i , is the first threshold crossing of the signal and it permits to perform the localisation of an AE source. The duration is the time from the first to the last threshold crossing of the signal. The amplitude is the peak voltage of the signal, while the number of oscillations is the number of threshold crossings by the signal. The threshold is selectable in the range between 100 μV and 6.4 mV.

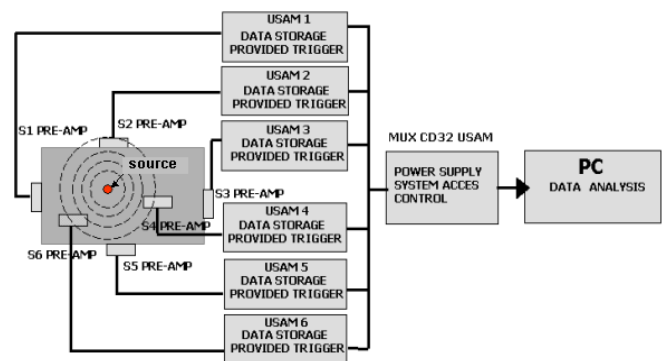


Figure 2. Acoustic emission measurement system.

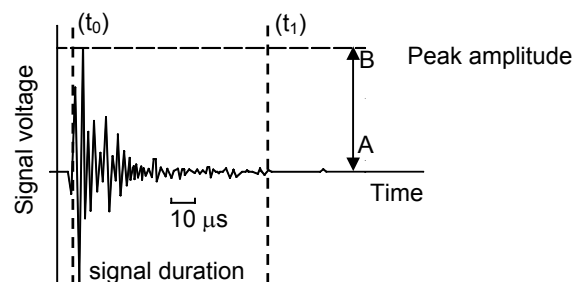


Figure 3. AE signal identified by the transducer.

3 ANALYSIS AND EARLY RESULTS

Considering FRC beams, two typical problems requiring rehabilitation are either too high deformations in service conditions, or an inadequate load carrying capacity.

In retrofitted structures the most frequently observed failure modes are (Arduini et al. 1997, Alaei & Karihaloo 2003, Leung 2004, Taljsten 1997): (i) FRP debonding or concrete ripping at the ends of the beam, depending on the adhesive properties; (ii) FRP debonding in proximity of flexural cracks; (iii) shear crack propagation in the concrete beam. As a consequence, fracture parameters of the interface and the nonlinear behavior of concrete are expected to exert a key role in the effectiveness of the retrofitting procedure. This is particularly true when ultimate conditions are analyzed. The FRP sheet insertion mainly causes two failure modes: (i) delamination between the FRP sheet and the concrete surface; (ii) a sudden shear failure starting from the cut-off edge of FRP and spreading through the beams.

In the set of FRC beams retrofitted with FRP sheets, the two cases mentioned in the Introduction have been assessed. In particular, specimen TR1 presents a sudden shear rupture localized near one of the two lower supports (Fig.4.a). The resulting crack growth crosses the whole cross-section, with a peak load approximately equal to 86 kN. For specimen TR2, the failure mode is a delamination with a peak load of about 65 kN. A number of strain gages are placed near the lower side of the beams and along the FRP sheets to record the strain distribution as a function of the applied load. Nevertheless, to evaluate the failure modes only the AE experimental data are considered.

From a qualitative observation of the failed specimens, the cracking pattern for TR1 shows the presence of several cracks along the whole intrados of the specimen. These cracks result into a sudden shear collapse shown in Figure 4a. For specimen TR2 we noticed a smaller number of cracks and a main crack with the mouth located at the end of the delaminated portion of the FRP sheet (Fig.4b).

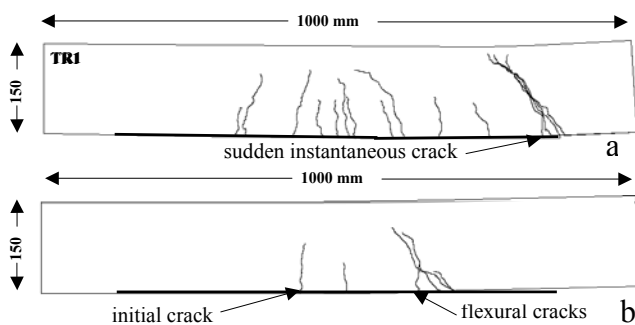


Figure 4. Cracking pattern for specimen TR1 (a) and specimen TR2 (b).

4 APPLICATION OF THE AE TECHNIQUE

Acoustic emissions are ultrasonic waves generated by a rapid energy release coming from discontinuities or cracks propagating in the materials subjected to a given stress state. Such waves propagate through the damaged solid in isotropic and homogeneous materials as straight rays moving, at a first approximation, with an isotropic velocity distribution, v . When they reach the outer surface, they are captured by piezoelectric sensors (Carpinteri, et al. 2006a, 2006b). During the loading test, the AE transducers have been positioned in order to investigate on the flexural crack growth and on the progress of the FRP-concrete delamination (Fig.5).



Figure 5. Three point bending tests and AE sensor positions.

4.1 AE energy evaluation

The AE energy released during crack growth is an important indicator of the damage process. The cumulative AE energy of the damage process is herein calculated considering that the energy of an AE signal is proportional to the square of the voltage. As a consequence, in our analysis we square and integrate in time the recorded transient voltage of each channel (see also Lin et al 1997):

$$E_c = \frac{1}{C} \sum_i \int_{t_0}^{t_1} A_i(t)^2 dt \quad (1)$$

In Eq.(1) the subscript i denotes the i_{th} event of the recorded transient voltage $A_i(t)$, while t_0 and t_1 represent the starting and ending times of the i_{th} transient voltage recording. C is a constant representing the resistance of the measuring circuit. For the energy calculation the threshold level of the signals recorded by the USAM, is fixed at $100\mu V$. This value is generally adopted by the authors in monitoring AE events in concrete (Carpinteri et al. 2006a). The maximum signal amplitude measured during the tests is about 12.8 mV. In Eq. (1) the cumulated AE energy E_c is obtained adding over all six channels the energy measured for each event.

during the damage process in specimens TR1 and TR2.

4.2 Localisation of AE sources

The first stage in the localisation method consists in recognising the data needed to identify the AE sources, and is followed by the triangulation procedure (Shah & Li, 1994). During the first stage, the groups of signals, recorded by the sensors, falling into time intervals compatible with the formation of micro-cracks in the analysed volume, are identified. These time intervals, of the order of micro-seconds, are defined on the basis of an *a priori* assured speed of transmission of the *P* waves and of the mutual distance between the applied threshold of $100\mu\text{V}$ of the non-amplified signal is appropriate to distinguish between *P*-wave and *S*-wave arrival times. In fact, *P*-waves are usually characterized by higher signal amplitudes (Shah & Li 1994, Carpinteri et al. 2006a).

In the second stage, when the formation of micro-cracks in a three-dimensional space is analysed, the triangulation technique can be applied if the signals recorded by at least five sensors fall into the compatible time intervals. According to this procedure, it is possible to define both the position of the micro-cracks in the volume and the speed of transmission of the *P*-waves. The localisation procedure can also be performed through numerical techniques using optimisation methods such as the Least Squares Method (LSM) (Carpinteri et al 2006b).

4.3 Moment tensor analysis

The approach applied in this study relies on the theoretical standpoint on the procedure defined by Shigeishi and Ohtsu (Shigeishi & Ohtsu 2001). This procedure characterizes the AE signal taking into account only the first arrival time of the *P*-waves. The elastic crack displacements $\mathbf{u}(\mathbf{x},t)$, at the points \mathbf{x} , which are the sources of the AE signals, are given by:

$$\mathbf{u}_i(\mathbf{x},t) = G_{ip,q}(\mathbf{x},\mathbf{y},t) m_{pq} * S(t), \quad (2)$$

where $G_{ip,q}(\mathbf{x},\mathbf{y},t)$ is the space derivative of the Green's function and the asterisk denotes the convolution operator. The Green's functions describe the elastic displacements $\mathbf{u}(\mathbf{x},t)$ due to a unit displacement applied in \mathbf{y} at time t . In the SiGMA procedure, the magnitude of the elastic displacements, proportional to the amplitudes $A(\mathbf{x})$ of the first *P*-waves reaching the transducers, are given by a modified expression of Eq. (2):

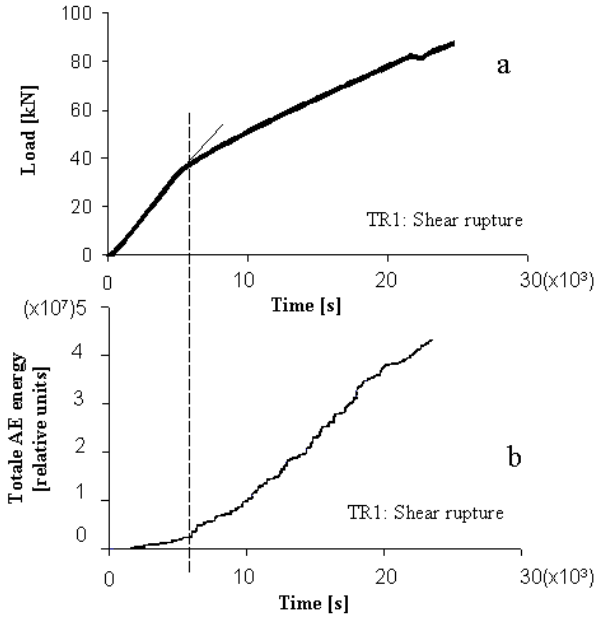


Figure 6. Load versus time diagram for TR1 (a); compared with the total AE energy cumulated during the test (b).

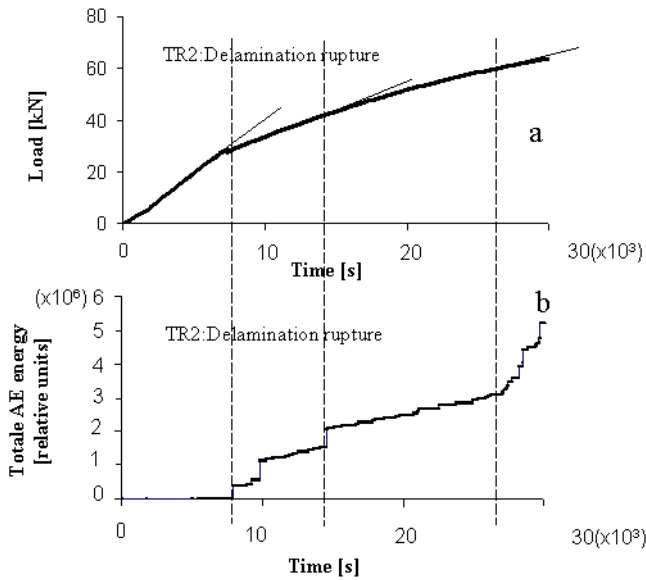


Figure 7. Load versus time diagram for TR2 (a); compared with the total AE energy cumulated during the test (b).

The total cumulative AE energy computed systematically increases with the different stages of damage, so it could be used to estimate the development of the fracture process. In Figures 6 and 7 the cumulative AE energy is plotted versus time and compared with the load carrying capacity during the three point bending tests for specimens TR1 and TR2.

The cumulative AE released energy exhibits a strong correlation with the decay of the mechanical properties of the specimens. These correspondences are indicated in Figures 6 and 7 with dashed lines. Sudden increases in the released energy level are related to appreciable drops of the Young's modulus

$$A(\mathbf{x}) = \frac{C_s \text{REF}(\mathbf{t}, \mathbf{r})}{R} (r_1 \ r_2 \ r_3) \begin{pmatrix} m_{11} & m_{12} & m_{13} \\ m_{21} & m_{22} & m_{23} \\ m_{31} & m_{32} & m_{33} \end{pmatrix} \begin{pmatrix} r_1 \\ r_2 \\ r_3 \end{pmatrix}, \quad (3)$$

where C_s is a calibration coefficient of the acoustic emission sensors and R is the distance between the AE source at point \mathbf{y} and the sensor located at point \mathbf{x} . R represents the distance between the source and the sensor. $\text{REF}(\mathbf{t}, \mathbf{r})$ is the reflection coefficient of the sensitivity of the sensor depending on the angle between the two direction of the two unit vectors \mathbf{r} and \mathbf{t} ; these vectors are respectively the unit vector along the R distance and the unit vector along the sensitivity sensor direction.

To represent the moment tensor, it is necessary to determine the six independent unknowns, m_{pq} . The amplitude of the signal $A(\mathbf{x})$ must be received by at least six AE sensors. Through an eigenvalue analysis of the moment tensor, it is possible to determine the type of crack localised. Referring each eigenvalue to the maximum one, it can be written:

$$\frac{\lambda_1}{\lambda_1} = X + Y + Z, \quad \frac{\lambda_2}{\lambda_1} = 0 - \frac{Y}{2} + Z, \quad \frac{\lambda_3}{\lambda_1} = -X - \frac{Y}{2} + Z, \quad (4)$$

where, $\lambda_1, \lambda_2, \lambda_3$ are the maximum, medium and minimum eigenvalues respectively, and X is the component due to shear, Y is the deviatoric tensile component, Z is the isotropic tensile component. Ohtsu classified an AE source with $X > 60\%$ as a shear crack (Mode II), one with $X < 40\%$ and $Y + Z > 60\%$ as a tensile crack (Mode I), and one with $40\% < X < 60\%$ as a Mixed Mode crack (Shigeishi & Ohtsu 2001). Moreover, from an eigenvector analysis it is possible to determine the unit vectors, \mathbf{l} and \mathbf{n} , which determine the directions of the displacement and the orientations of the crack surface.

4.4 Procedure for 3D AE analysis

Using the USAM® equipment the authors have fine-tuned a computer-based procedure including the AE source location and the moment tensor analysis. This procedure is implemented in an automatic AE data processing program coded in MAPLE 9.5 (FORTRAN77), whose overall flowchart is shown in Figure 8. The whole routine is divided into three parts automatically executed: (i) recognition and identification; (ii) location and moment tensor analysis; (iii) automatic translation of 3D AE pattern. The final output of the code returns a complete description of damage characterization and evolution. The 3D AE source positions obtained are overlapped to the 3D crack patterns deduced from the observation of the cracking map.

In both TR1 and TR2 specimens, damage localization, typology and direction vector of the

crack are shown in Figures 9 and 10. The position of each emission source, the typologies for Mode I, Mode II and Mixed Mode and the crack direction for Mode I and Mode II are represented according to the notation listed in Table 3.

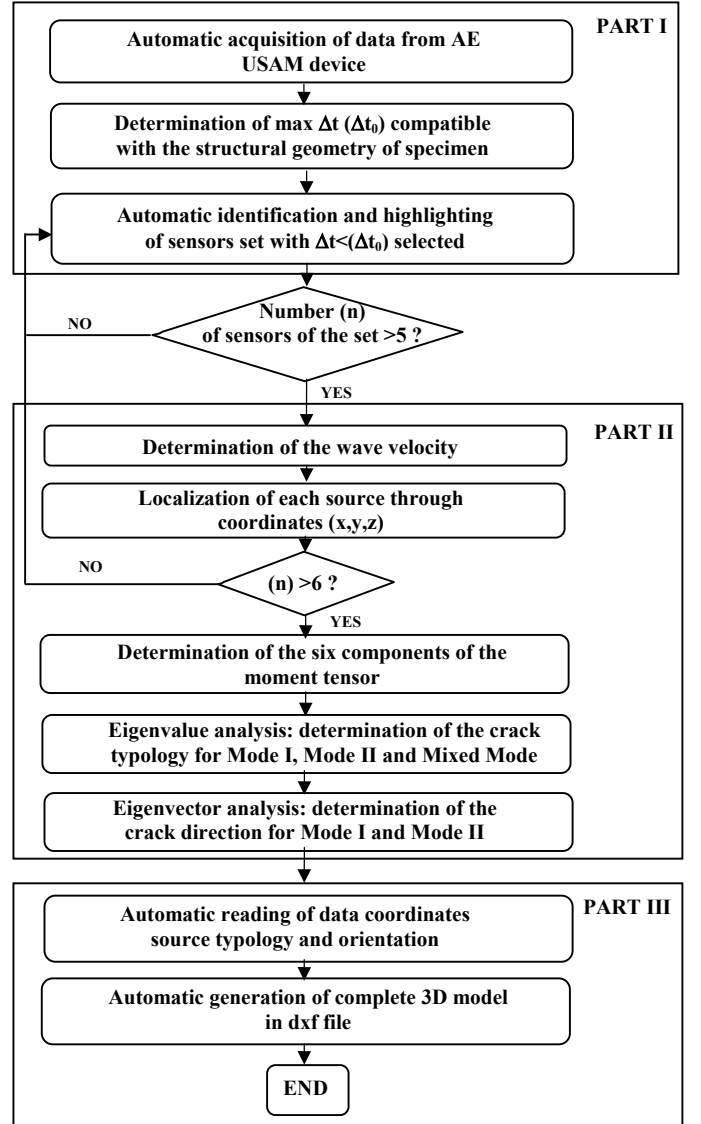


Figure 8. Flowchart of the localization and moment tensor analysis program.

Table 3: Markers of AE sources and labels identifying crack typology and direction.

Crack Position	●
Crack Typology	
Mode I	⊖
Mode II	⊗
Mixed Mode	⊗
Crack Direction	/

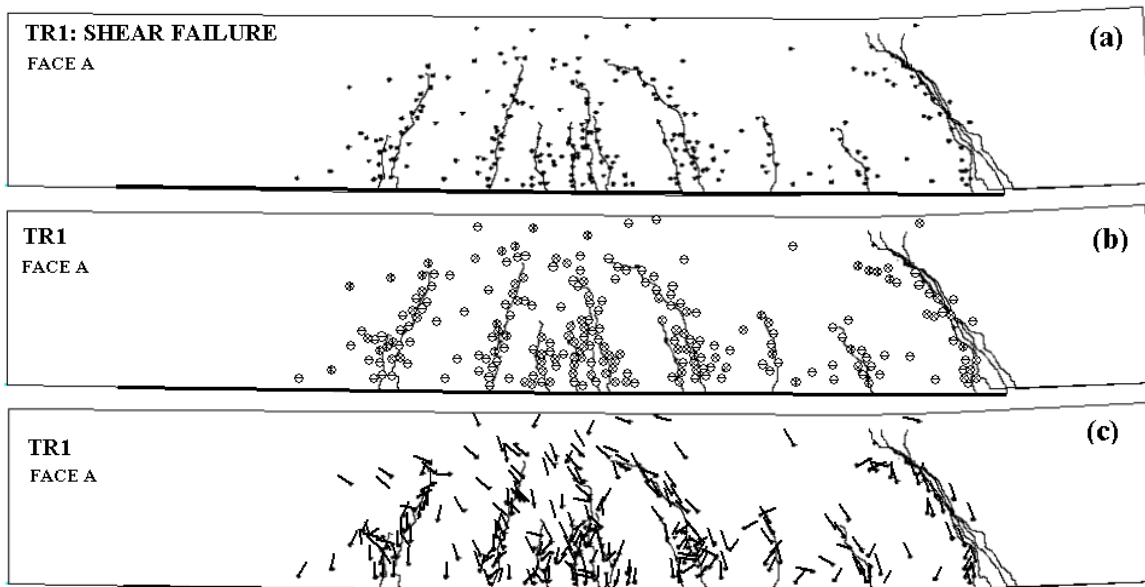


Figure 9. AE sources in TR1 specimen: (a) Localization, (b) crack type for Mode I, Mode II and Mixed Mode, (c) crack direction for Mode I and Mode II.

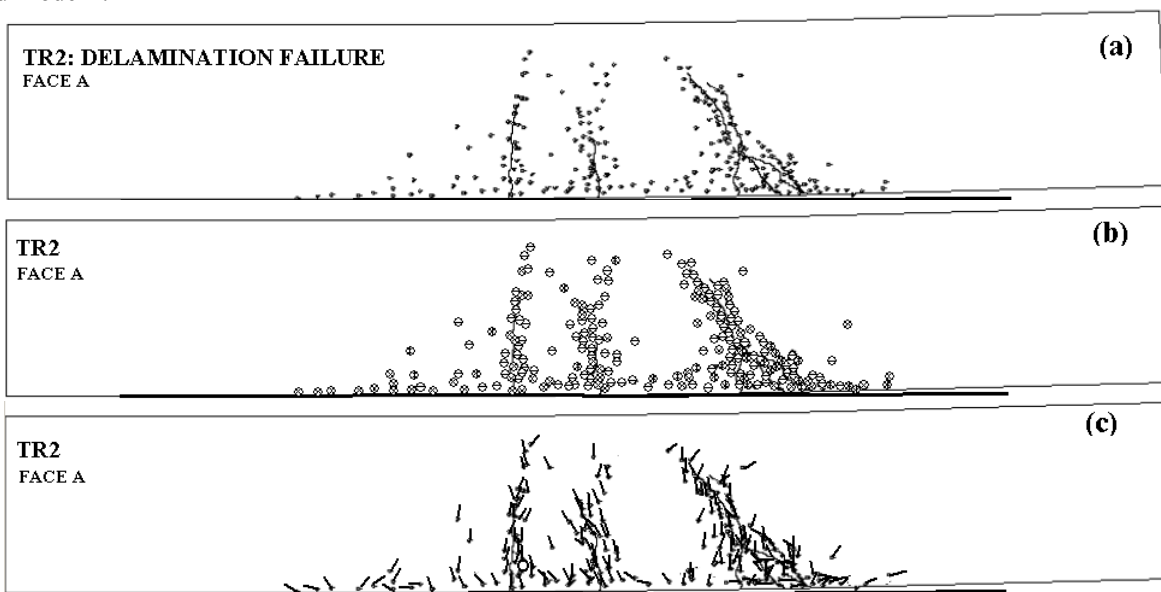


Figure 10. AE sources in TR2 specimen: (a) Localization, (b) crack type for Mode I, Mode II and Mixed Mode, (c) crack direction for Mode I and Mode II.

4.5 Moment tensor analysis and results

Crack types of AE sources obtained under three point bending tests were analysed as shown in Figures 11 and 12. As regards specimen TR1 (shear rupture), we observe that the percentage of shear cracks (Mode II) becomes progressively comparable with the percentage of tensile cracks (Mode I) during the test (Fig.11). In fact, beyond a certain distance from the midpoint of the beam, the cracking map shown in Figure 9 denotes that the micro-cracks propagate along oblique crack planes. On the other hand, for the TR2 specimen failed due to delamination, Mode I cracks are prevalent. At the end of the test, they consist in more than 50% of the total number of the localized events (Fig.12). This behaviour can be interpreted by noting that, during the progress of damage, the specimen experienced flexural cracks near the mid-span position, that are typically

classified as Mode I cracks. The effect of delamination has also been quantified by analysing a set of events located in a portion corresponding to a volume of $25 \times 1000 \times 150 \text{ mm}^3$ along the intrados of the specimens. This volume has been considered as the damage zone involved in the delamination process between concrete and FRP. As far as the TR1 specimen is concerned, the localized events in this representative zone are less than 20% of the total number of events at the end of the test (see Fig. 13). On the other hand, for the TR2 specimen (see Fig.14) the percentage of events coming from this zone is significantly higher (50%) than that observed for the TR1 specimen. Considering the total amount of the localized events during the tests, we highlight that the delamination process in the TR2 specimen started earlier than in the TR1 specimen, as confirmed by the comparison between the percentages of the localized events falling in the

delamination process zone. The difference in the failure modes is due to the effectiveness of the bonding between the FRP sheet and the concrete surface for the two specimens.

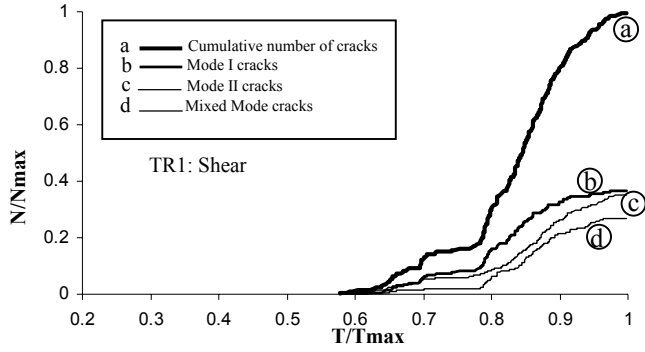


Figure 11. Cumulative number of cracks of different types and total number of cracks for specimen TR1.

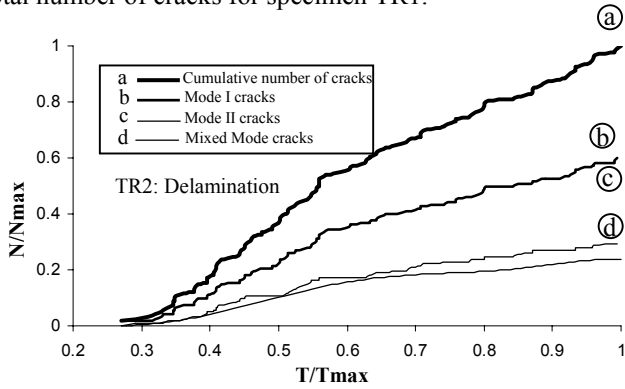


Figure 12. Cumulative number of cracks of different types and total number of cracks for specimen TR2.

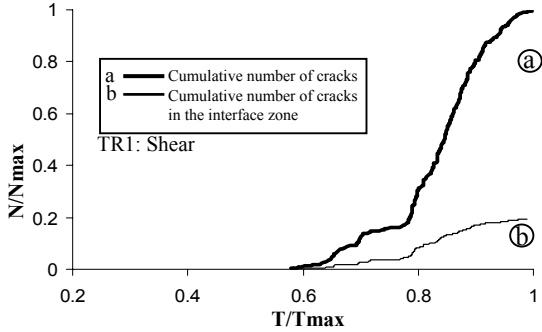


Figure 13. Cumulative number of cracks located in the delamination process zone and total cumulative number of cracks for specimen TR1.

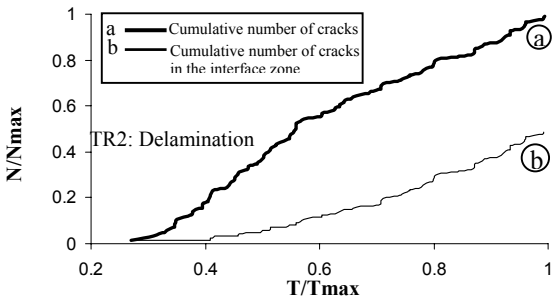


Figure 14. Cumulative number of cracks located in the delamination process zone and total cumulative number of cracks for specimen TR2.

5 STATISTICAL DISTRIBUTION OF AE EVENTS

By analogy with seismic phenomena, in the AE technique the magnitude may be defined as follows:

$$m = \text{Log}_{10} A_{\max} + f(r), \quad (5)$$

where A_{\max} is the amplitude of the signal expressed in μV , and $f(r)$ is a correction coefficient whereby the signal amplitude is taken to be a decreasing function of the distance r between the source and the AE sensor. The empirical Gutenberg-Richter's law (Richter 1958) provides:

$$\text{Log}_{10} N(\geq m) = a - bm \text{ or } N(\geq m) = 10^{a-bm}, \quad (6)$$

where N is the cumulative number of earthquakes with magnitude $\geq m$ in a given area and a specific time-range, whilst a and b are positive constants varying from a region to another and from a time interval to another. Eq. (6) has been used successfully in the AE field to study the scaling laws of AE wave amplitude distribution. This approach highlights the similarity between structural damage phenomena and seismic activities in a given region of the earth, extending the applicability of the Gutenberg-Richter's law to Structural Engineering. According to Eq. (6), the “ b -value” stands for the slope of the regression line in the “log-linear” diagram of AE signal amplitude distribution. This parameter changes systematically at different times in the course of the damage process and therefore can be used to estimate damage evolution modalities. Scale effects on the size of the cracks identified by the AE technique entail, by analogy with earthquakes (Carpinteri et al. 2006b, Richter 1958), the validity of the following relationship:

$$N(\geq L) = cL^{-2b}, \quad (7)$$

where N is the cumulative number of AE events generated by cracks having a characteristic size $\geq L$, c is the total number of AE events and $D = 2b$ is the noninteger (or fractal) exponent of the distribution. The cumulative distribution (7) is substantially identical to the one proposed by Carpinteri (Carpinteri 1986, 1994), according to which the number of cracks with size $\geq L$ contained in a body is given by:

$$N^*(\geq L) = N_{tot} L^{-\gamma}. \quad (8)$$

In Eq. (8), γ is an exponent reflecting the disorder, i.e., the crack size scatter, and N_{tot} is the total number of cracks contained in the body. By equating distributions (7) and (8), we find that: $2b = \gamma$. At the final collapse, when the size of the largest crack is proportional to the largest size of the body, function (8) is characterised by an exponent $\gamma = 2$, corresponding to $b = 1$. In

(Carpinteri 1994) it is also demonstrated that $\gamma = 2$ is a lower limit. This corresponds to the minimum value $b = 1$, observed experimentally when the bearing capacity of a structural member is exhausted. By applying these concepts to the “ b -value” analysis of specimens TR1 and TR2, it can be seen that the TR1 specimen exhausted its bearing capacity during the loading test, with the formation of cracks of a size comparable to that of the specimen (b -value $\cong 1$). On the other hand, the TR2 specimen, characterised by a flexural cracking pattern, was still having a reserve of strength before reaching the final collapse (b -value = 1.57). The “ b -value” for the two specimens is shown in Figure 15.

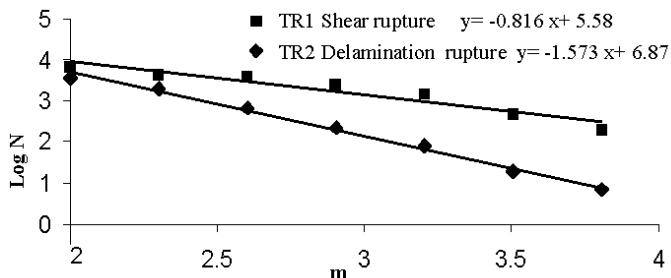


Figure 15. Determination of the “ b -value” at the end of the tests on the specimens TR1 and TR2.

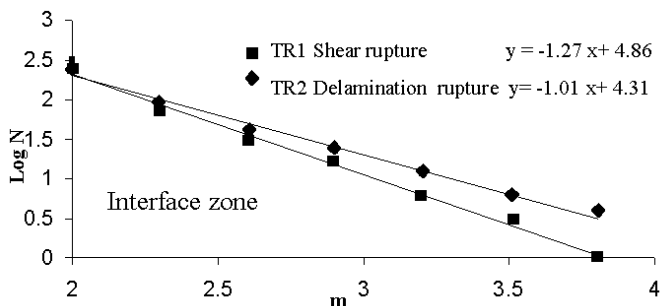


Figure 16. Determination of the “ b -value” at the end of the tests of the specimens TR1 and TR2, and in relation to the delamination process zone.

In Figure 16 we propose a comparison between the two b -values of the two specimens considering only the events located in the delamination process zone previously defined. It can be realized that in the delamination process zone the TR1 specimen presents a b -value ($=1.27$) higher than that of the TR2 specimen ($=1.01$). This fact can be ascribed to the occurrence of delamination failure observed in the TR2 specimen.

6 CONCLUSIONS

A set of FRC beams was cast and subsequently retrofitted with FRP sheets at the Fracture Mechanics Laboratory of the Politecnico di Torino. On the basis of AE monitoring, loading tests have been conducted to analyse the cracking progression in the beams. The experimental results demonstrate the effectiveness of the AE technique for the interpretation and prediction of the failure modes in these composite structures.

ACKNOWLEDGEMENTS

The financial support provided by the Italian Ministry of University and Research (MIUR) is gratefully acknowledged. The authors would like to thank Mr. V. Di Vasto for the technical support and MS eng. R. Gottardo, Technical Manager of the D.L. Building System DEGUSSA Construction Chemicals Italia, for providing the FRP sheets used in the testing programme.

REFERENCES

- Alaee, F.J. & Karihaloo, B.L. 2003. Fracture model for flexural failure of beams retrofitted with CARDIFRC. *ASCE Journal of Engineering Mechanics* 129:1028-1038.
- Arduini, M. Di Tommaso, A. Nanni, A. 1997. Brittle failure in FRP plate and sheet bonded beams. *ACI Structural Journal* 94:363-370.
- Carpinteri, A. 1986. *Mechanical Damage and Crack Growth in Concrete: Plastic Collapse to Brittle Fracture*, Dordrecht: Martinus Nijhoff Publishers.
- Carpinteri, A. 1989. Cusp catastrophe interpretation of fracture instability. *Journal of the Mechanics and Physics of Solids* 37: 567-582.
- Carpinteri, A. 1994. Scaling laws and renormalization groups for strength and toughness of disordered materials. *International Journal of Solids and Structures* 31: 291-302.
- Carpinteri, A. Lacidogna, G. Paggi, M. 2006a. Acoustic emission monitoring and numerical modelling of FRP delamination in RC beams with non-rectangular cross-section. *Materials and Structures (RILEM)*, in press.
- Carpinteri, A. Lacidogna, G. Niccolini, G. 2006b. Critical behaviour in concrete structures and damage localization by acoustic emission. *Key Engineering Materials* 312: 305-310.
- Colombo, S. Main, I.G., Forde, M.C. 2003. Assessing damage of reinforced concrete beam using b -value analysis of acoustic emission signals. *ASCE Journal of Materials in Civil Engineering* 15: 280-286.
- Grosse, C.U. Reinhardt, H.W. Finck, F. 2003. Signal based acoustic emission techniques in civil engineering. *ASCE J Mater Civil Eng.* 15:274-279.
- Leung, C.K.Y. 2004. Delamination failure in concrete beams retrofitted with a bonded plate. *Journal of Materials in Civil Engineering* 13:106-113.
- Lin, C.K. Berndt, C. Leigh, S. Murakami, K. 1997. Acoustic Emission Studies of Alumina-1 3% Titania Free-Standing Forms during Four-Point Bend Tests. *Journal of American Ceramic Society* 9: 2382-2394.
- RILEM TC TDF-162, 2002. Test and design methods for steel fiber reinforced concrete. Bending test – Final Recommendation,. *Materials and Structures (RILEM)* 35: 579-582.
- RILEM FMC1, 1985. Determination of the fracture energy of mortar and concrete by means of three-point bend tests on notched beams. *Materials and Structures (RILEM)*. 18: 285-290.
- Richter, C. F. 1958. *Elementary Seismology*. S. Francisco and London: W.H. Freeman and Company.
- Shah, S P. & Li, Z. 1994. Localisation of microcracking in concrete under uniaxial tension. *ACI Materials Journal* 91: 372-381.
- Shigeishi, M. & Ohtsu, M. 2001. Acoustic emission moment tensor analysis: development for crack identification in concrete materials. *Construction and Buildings Materials* 15: 311-319.
- Taljiesten, B. 1997. Strengthening of beams by plate bonding. *ASCE Journal of Materials in Civil Engineering* 9:206-212.